Available online at www.sciencedirect.com
SCIENCE DIRECT®
Journal of Magnetic Resonance 172 (2005) 254–267
JMR Journal of Magnetic Resonance
www.elsevier.com/locate/jmr

The solution conformation of triarylmethyl radicals

M.K. Bowman[a,*], C. Mailer[b], H.J. Halpern[b]

[a] *Structural Biology and Microimaging, Pacific Northwest National Laboratory, Richland, WA 99352-0999, USA*
[b] *Department of Radiation and Cellular Oncology, Center for EPR Imaging In Vivo Physiology, Chicago, IL 60637, USA*

Received 8 June 2004; revised 21 October 2004
Available online 21 November 2004

Abstract

Hyperfine coupling tensors to ^{1}H, ^{2}H, and natural abundance ^{13}C were measured using X-band pulsed electron nuclear double resonance (ENDOR) spectroscopy for two triarylmethyl (trityl) radicals used in electron paramagnetic resonance imaging and oximetry: methyl tris(8-carboxy-2,2,6,6-tetramethyl-benzo[1,2*d*:4,5-*d*′]bis(1,3)dithiol-4-yl) and methyl tris(8-carboxy-2,2,6,6-tetramethyl(-d_3)-benzo[1,2*d*:4,5-*d*′]bis(1,3)dithiol-4-yl). Quantum chemical calculations using density functional theory predict a structure that reproduces the experimentally determined hyperfine tensors. The radicals are propeller-shaped with the three aryl rings nearly mutually orthogonal. The central carbon atom carrying most of the unpaired electron spin density is surrounded by the sulfur atoms in the radical and is completely shielded from solvent. This structure explains features of the electron spin relaxation of these radicals and suggests ways in which the radicals can be chemically modified to improve their characteristics for imaging and oximetry.

Keywords: Trityl radical; ENDOR; Pulsed EPR

1. Introduction

The trityl family of triarylmethyl radicals has recently come into use in a number of magnetic resonance applications because of their favorable relaxation and spectral properties. These radicals, as typified by **I**, (see Scheme 1), methyl tris(8-carboxy-2,2,6,6-tetramethyl-benzo[1,2*d*:4,5-*d*′]bis(1,3)dithiol-4-yl), have a single, narrow electron paramagnetic resonance (EPR) line even at high fields and have long relaxation times in fluid solution, which make them useful electron spins for some classes of dynamic nuclear polarization measurements [1–4]. They also have good chemical stability and are not generally broadened by interaction with proteins and other biological molecules, making them attractive probes for biological EPR imaging and EPR oximetry applications [5–11].

The trityl family has two major sites for chemical variation that can be used to adjust their chemical or spectroscopic properties for specific uses: the *para* position on the phenyl rings or the methylene bridge in the five-membered rings. An improved knowledge of the electronic and physical structure of the trityl radicals in solution would help guide development of improved trityl radicals and would aid in understanding the response of current trityl radicals to molecular oxygen and to other paramagnetic species, and the transfer of polarization to solvent nuclei in liquid phase dynamic nuclear polarization (DNP). The chemical structure of **I** is usually drawn as if the molecules were planar. However, the substituted phenyl rings are far too bulky to allow three coplanar phenyl rings around the central carbon. The rings must twist substantially out of plane, decreasing conjugation of the π-electron system. The conformation adopted by **I** in solution will have a large effect on the unpaired spin density distribution and on the ability of dissolved species such as molecular oxygen and paramagnetic metal ions to interact with the

* Corresponding author. Fax: +1 509 376 2303.
E-mail address: michael.bowman@pnl.gov (M.K. Bowman).

1090-7807/$ - see front matter © 2004 Elsevier Inc. All rights reserved.
doi:10.1016/j.jmr.2004.10.010

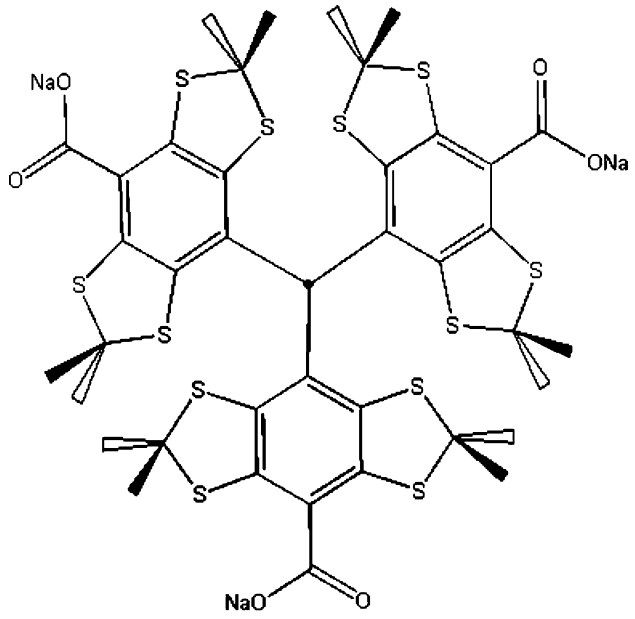

I

Scheme 1.

unpaired electron spin and to cause relaxation or broadening of the EPR spectral lines. In addition, fluctuations in the conformation and transient hydrogen bonds formed with solvent have the potential to modulate the unpaired spin distribution and contribute to intrinsic EPR linewidth.

The conformation of free radicals in solution is often probed experimentally using proton hyperfine interactions to map out the unpaired spin density distribution in the radical. The trityl radicals of most interest for EPR oximetry are purposely designed to minimize or eliminate hyperfine couplings to protons, leaving few sites on **I** that can be probed. An alternative probe of the unpaired electron spin density is provided by the carbons which form most of **I**. This requires measurement of the hyperfine couplings of ^{13}C, the only stable carbon isotope with a nuclear spin, either by EPR or by electron nuclear double resonance (ENDOR). Although the natural abundance of the ^{13}C isotope is only 1.11%, there are two factors that make it practical to measure the ^{13}C hyperfine interactions of the trityl radical in natural abundance samples. The first factor is that **I** has many carbon atoms in it arranged in a few chemically equivalent groups with degeneracies of 3, 6 or 12. Thus, a substantial fraction, about 36%, of radicals in the sample is naturally 'labeled' with ^{13}C. The second favorable factor for the measurement of ^{13}C ENDOR is the fact that the ^{13}C hyperfine splittings for several of the carbon positions are much larger than the EPR linewidth of the 'unlabeled' radical. Measurements can be cleanly made of only the naturally 'labeled' **I** without interference from 'unlabeled' **I**. These factors allow a detailed experimental characterization of the electronic structure of **I** based on both the proton and carbon hyperfine interactions.

We report here on an EPR, ENDOR, and quantum chemical study of the simple, symmetric trityl radical **I**. The results indicate a single structure in both liquid and frozen solutions in which the three phenyl rings are twisted 51° out of plane so that the rings are almost mutually perpendicular, making an angle of 84.5° to each other. This conformation shields the central carbon atom bearing the majority of the unpaired electron spin density from the solvent and may be responsible for rendering **I** relatively insensitive to most interactions with its environment.

2. Experimental

2.1. EPR and ENDOR

CW EPR spectra were obtained with a spectrometer operating at 255 MHz. The bridge has a reference arm and uses quadrature RF detection [12]. One channel detects the modulated RF EPR signal that is passed to the phase sensitive detector, and the other is used in a DC Pound automatic frequency control (AFC) system [13]. One required extra feature of the bridge is a correction for frequency drift of the EPR resonator. The resonator drifts in frequency by tens of kHz in the course of a measurement. Because resonance position changes by 0.1 μT for a 2.8 kHz frequency change, such a slow frequency drift would cause broadening in the recorded EPR spectra and would prevent accurate analysis of the hyperfine splittings. The frequency drift correction operates by measuring the moment-to-moment RF frequency of the 250 MHz source oscillator as it is adjusted by the AFC. These frequency data are used to correct for the shifts in resonance position.

A one loop-one gap resonator with a diameter of 19 mm and length 15 mm was used. The computer-controlled DC magnet field has a high absolute stability of 0.05 μT which represents a fractional stability of 6 ppm relative to the center magnetic field of only 9 mT. The ~5 kHz Zeeman modulation is produced by a Helmholtz coil pair with less than 0.02 μT (20 ppm/cm) variation over a 1 cm diameter region along the resonator axis (RF B_1 field direction). For accurate simulations of the spectra careful calibration of the modulation amplitude was done.

Pulsed EPR measurements were performed at X-band on a Bruker ESP 380E EPR spectrometer with DICE ENDOR accessory and a Flexline CFG-935 helium flow cryostat and Flexline ENDOR resonator. Microwave frequency was measured with an EIP 575B microwave counter. A 20 W ENI 320L RF amplifier was used for Mims ENDOR measurements and a 500 W ENI A-500 amplifier was used for coherence

transfer ENDOR of protons based on the Mims ENDOR sequence and using time proportional phase incrementation (TPPI) as described by Höfer [14] to separate the higher multiple quantum orders. Pulsed EPR measurements of frozen solutions were made with the expectation that the hyperfine anisotropy could provide additional checks on the accuracy of the quantum chemical calculations.

The echo induced EPR spectrum [15] was measured with a $\pi/2$–τ–π–τ-detect sequence where $\pi/2$ and π indicate the turning angles of the respective microwave pulses separated by a time τ. A simple phase cycle was used to remove unwanted signals and to correct baseline offset. The phase of the first pulse was set to 0° and 180° on successive scans that were then subtracted from each other. The Mims ENDOR spectrum [16] was measured with the sequence $\pi/2$–τ–$\pi/2$–RF(T)–$\pi/2$–τ-detect. The RF frequency was swept and the RF pulse length is T. The phase of the second microwave pulse was set to 0° and 180° on successive scans that were then subtracted from each other.

The electron nuclear quadruple resonance (ENQOR) spectrum [17] was measured with a variation of the Mims ENDOR sequence, that is, $\pi/2$–τ–$\pi/2$–RF1–RF2–π–RF2′–RF1′–$\pi/2$–τ-detect. Phase cycling of the second microwave pulse was used as for Mims ENDOR. The RF pulses have equal length. RF1 and RF1′ indicate the same frequency which is different from that of RF2 and RF2′. The amplitude of one of the RF pulses in each pair RFn and RFn' is always zero. Additional phase cycling was superimposed on that of the microwave pulses depending on whether RF1 and RF2 have the same or different amplitudes.

For coherence transfer ENDOR [14,16], the single RF pulse was replaced by a pair of high-power RF pulses with turning angles of $\pi/2$ for the protons. The frequency of the RF pulses was the same but their relative phase was incremented with the time between the RF pulses at a rate of 1.44°/ns. The total time between the second and third microwave pulses was kept constant and the same phase cycling used as for Mims ENDOR. First RF pulse produces proton coherences which then evolve and are converted by the second RF pulse back to population differences for detection by the electron spin echo. The TPPI produces a phase modulation that is proportional to that multiple quantum order of the proton coherence. Fourier transformation of such a coherence transfer ENDOR signal produces an ENDOR spectrum with the different multiple quantum orders offset in frequency.

The Davies ENDOR spectrum [16] was measured with the sequence π–RF(T)–$\pi/2$–τ–π–τ-detect. The RF frequency was swept and the RF pulse length is T. The phase of the second microwave pulse was set to 0° and 180° on successive scans that were then subtracted from each other.

In the pulsed ENDOR measurements, the pulse widths, delays, amplitudes, and the magnetic field were adjusted to emphasize a particular feature in the ENDOR spectrum. That feature was then used to determine one of the many hyperfine tensor elements. The hyperfine tensors were constructed and assigned to specific positions in **I** on the basis of the tensors obtained from the quantum chemical calculations and the experimental EPR spectra. Precise fitting of experimental ENDOR spectra is not practical because it requires more information concerning the range of conformations of **I** present in the frozen solution samples and the consequent range of hyperfine tensor elements than is available.

2.2. Computational

Calculations of the hyperfine couplings were performed using the Gaussian 98 suite of programs [18]. The calculations were carried out on an 8 CPU Silicon Graphics Origin 2000 computer. The structure of **I** was optimized without the use of symmetry using density functional theory with the B3LYP functional, first with a 6-21G basis set and then with the 6-31G basis set. The optimized 6-31G structure was then used for calculations with other basis sets. The structure of **I** was modeled starting with the carboxyl groups ionized and three H_3O^+ in order to have a neutral system and to avoid having naked counter ions. The optimized structures have protonated carboxyl groups that are hydrogen bonded to a water molecule. The hyperfine tensors were calculated using the EPR Properties keyword of Gaussian.

ENDOR spectra were simulated using the program EPR-NMR (Department of Chemistry, University of Saskatchewan, Saskatoon, SK).

3. Results

3.1. Liquid phase CW EPR

The CW EPR spectrum of **I** is dominated by a single, narrow line. This is one of its attractions for magnetic resonance applications. However, there are a number of weak flanking lines from those radicals that contain a ^{13}C nucleus (natural abundance 1.11%). With 40 carbons in **I**, a random distribution would give 64% of the trityl radicals with no ^{13}C, 28% with one, 6.3% with 2, and 0.9% with 3. Each equivalent carbon position produces a pair of lines with equal intensity split approximately symmetrically about the central EPR line and an intensity directly related to its degeneracy in **I**. The splitting directly gives the isotropic hyperfine interaction after correction for second-order shifts that are noticeable in the 255 MHz EPR measurements. The line shape of the central line was carefully fit using an analysis program that completely corrects for Zeeman mod-

Table 1
Isotropic hyperfine couplings of **I** from liquid phase CW EPR measurements and DFT calculations with the 6-311G** basis set

Nucleus	A_{iso} (MHz)			Degeneracy	Assignment
	255 MHz	X-band	Calculated		
^{13}C		67.1	61.60	1	Central carbon
^{13}C	32.09	31.7	-32.51 ± 0.04	3	1-Phenyl
^{13}C	25.30	25.4	25.66 ± 0.10	6	2,6-Phenyl
^{13}C	9.41	—	5.90 ± 0.04	3	4-Phenyl
^{13}C	6.60	—	-5.07 ± 0.05	6	3,5-Phenyl
^{13}C	3.57	—	-3.42 ± 0.03	3	Carboxyl
^{13}C[a]	0.494 ± 0.036	—	-0.51 ± 0.01	6	Methylene bridge
^{13}C[a]	0.066 ± 0.001	—	0.083 ± 0.003 0.031 ± 0.001	12	Methyl carbons
^{1}H[a]	0.033 ± 0.001 (0.006 ^{2}H)	—	Average: -0.050 (^{1}H)	36	Methyl protons
^{1}H	—	—	-0.11 ± 0.003	3	Carboxyl protons[b]
^{33}S	—	—	0.48 ± 0.03	6	2,6-Phenyl
^{33}S	—	—	-0.42 ± 0.01	6	3,5-Phenyl

EPR measurements determine only the absolute value of the hyperfine coupling constant while the DFT calculations also give the sign of the coupling.

[a] Splittings were not resolved and couplings were obtained from fitting the line shape of the central line. The values of the hyperfine couplings are highly correlated and the estimated uncertainties are more relevant to the second moment than for the individual couplings. The uncertainty in the resolved hyperfine couplings is a fraction of the ~0.076 MHz CW EPR linewidth of the deuterated radical.

[b] Protons hydrogen bonded to the carbonyl oxygen have smaller, −0.01 MHz, calculated isotropic hyperfine couplings.

ulation frequency and amplitude and also models the resolved and unresolved hyperfine patterns expected from the structure (Table 1) [19]. Equivalent results, Table 1, were obtained in room temperature CW EPR measurements at 255 MHz on 1 mM deuterated **I** in water and at X-band on 1.5 mM deuterated **I** in perdeuterated methanol. The degeneracies listed in Table 1 are derived from the relative EPR line intensities. There appears to be sufficient conformational mobility of **I** to make the potentially inequivalent sets of methyl groups magnetically equivalent in solution.

The ^{13}C hyperfine lines from central methyl carbon were not measured in the 255 MHz EPR spectra because narrow, high-resolution field sweeps were used to focus on the smaller splittings of the remaining carbons. Although ^{13}C hyperfine splittings were readily observed, there was no trace of hyperfine splittings from ^{33}S which has a natural abundance of 0.75% and $I = 3/2$. There should be two sets of ^{33}S hyperfine splittings from the 2,6- and the 3,5-phenyl positions, respectively, each with a degeneracy of 6. No such splittings were observed, most likely because the large quadrupole moment of ^{33}S cause rapid nuclear relaxation and broaden the hyperfine lines beyond detection.

3.2. Solid-state EPR

The CW EPR spectrum of frozen solutions of **I** are also dominated by a single, narrow line. The sharp ^{13}C hyperfine lines are replaced by the full hyperfine powder patterns for each ^{13}C position in the radical. Each one has the form of a high-field ^{13}C powder ENDOR spectrum centered near the EPR frequency of **I**. The relative intensity of each hyperfine powder pattern is determined by the degeneracy of that carbon position in the radical and by the relative spectral dispersion or hyperfine anisotropy. Thus, the more anisotropic the coupling the weaker its intensity in the spectrum. Only a few of the larger hyperfine couplings were well resolved in either CW EPR or ESE detected EPR spectra, Fig. 1, giving values in Table 2. The spectra were consistent with roughly axial hyperfine tensors. There is one well-re-

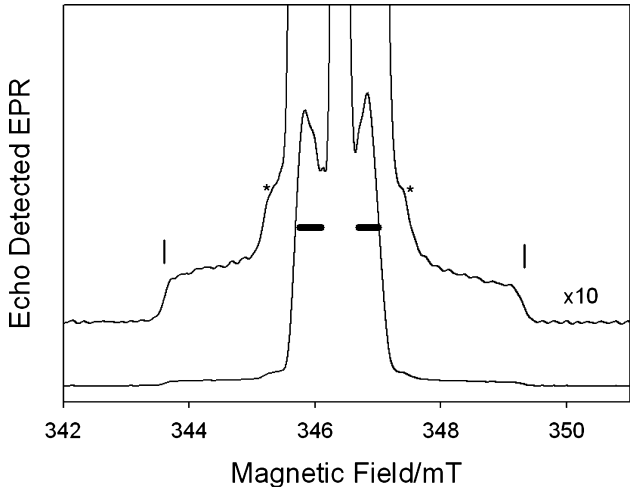

Fig. 1. The echo detected EPR spectrum of 1.5 mM deuterated **I** in deuterated methanol at 60 K at 9.707 GHz. The pulse repetition rate was 122 Hz, and the interpulse delay in the two-pulse echo sequence was 800 ns with microwave pulses of 256 and 512 ns corresponding to π/2 and π pulses, respectively, and the entire echo was integrated. The main peak of the trityl radical saturated the receiver and is not shown. The shoulders marked by vertical lines are the $A_{\|}$ features with a splitting of 160.1 MHz in the first entry in Table 2; the horizontal bars indicate the overlapping features in the second and third entries in Table 2; and the stars mark shoulders assigned to an impurity in the sample as discussed in the text.

Table 2
Hyperfine tensors of **I** from solid-state EPR and ENDOR measurements and from DFT calculations

Nucleus	CW EPR hyperfine coupling (MHz)		ENDOR hyperfine coupling (MHz)		Gaussian-98 hyperfine coupling (MHz)	
	$A_\parallel$	$A_\perp$	$A_\parallel$	$A_\perp$	A_1	A_2, A_3
Central ^{13}C	160.1	(20.6)	—	—	176.7	4.1, 4.1
1-Phenyl ^{13}C	39.6	29.5	40.3	27.8	−42.1	−28.5, −26.9
2,6-Phenyl ^{13}C	37.7	17.0	36.7	18.0	37.0	20.8, 19.1
4-Phenyl ^{13}C	15.6	(6.3)	12.7	7.6	16.8	0.9, 0.0
3,5-Phenyl ^{13}C	—	—	10.5	5.4	−10.2	−3.1, −1.9
Carboxyl ^{13}C	—	—	—	—	−3.7	−3.3, −3.2
Bridging ^{13}C	—	—	−0.4[a]	−0.8[a]	−0.18	−0.66, −0.69
Methyl ^{13}C	—	—	0.16	0.0	0.24 0.26	−0.05, −0.05, 0.01, −0.05
Methyl ^{1}H	—	—	1.0[b]	−0.5[b]	0.4–1.1	−0.2 to −0.6
Carboxyl ^{1}H[c]	—	—	—	—	0.62	−0.45, −0.50
Impurity	64.4	50.5	—	—	—	—

The calculated values for the methyl protons show the range of values while the methyl ^{13}C couplings for axial and equatorial groups are reported on different lines. The experimental spectra did not allow resolution of the $A_\perp$. The CW EPR values reported in parentheses were calculated from the measured $A_\parallel$ and A_{iso} but were not directly observed in the spectra.

[a] The sign of the hyperfine couplings were determined by ENQOR relative to the methyl ^{1}H couplings which were assumed to be dominated by a nearly point–dipole interaction with spin density on the central carbon atom.

[b] Extrema from features in the coherence transfer ENDOR spectrum.

[c] The anisotropic part of the calculated hyperfine tensor from protons hydrogen bonded to the carbonyl oxygen is slightly smaller than for the –OH proton.

solved shoulder in both the CW and ESE detected spectra that has small anisotropy and rather weak intensity considering its small anisotropy. The calculated isotropic hyperfine coupling of 55.1 MHz is quite different from those measured in the liquid phase and is consequently assigned to a trace impurity in the sample that is noticeable only because of its large, nearly isotropic coupling.

Overlap, from the wings of the intense EPR line from radicals that contain no ^{13}C, obscures the region expected to contain the features from the small ^{13}C hyperfine tensor components. The largest splitting observed, $A_\parallel = 160.1$ MHz, must correspond to the largest isotropic coupling of 67.1 MHz because all other features in the solid-state EPR spectrum have splittings less than this isotropic coupling. The other two principal values of this hyperfine tensor would average 20.6 MHz and lie buried under the much more intense central portion of the solid-state EPR spectrum.

3.3. Pulsed ENDOR

3.3.1. Hydrogen Mims ENDOR

The proton Mims ENDOR spectrum of **I** is narrow and contains partially resolved features that shift noticeably as the RF pulse amplitude and length are varied. However, the shape of the Mims ENDOR spectrum does not depend on temperature. Spectra measured between 4.5 and 60 K can be superimposed and show no indication that methyl group dynamics alters the spectrum over this temperature range.

In a typical spectrum, Fig. 2, there is a set of broad lobes split by ~800 kHz and a pair of sharper peaks split by ~300 kHz. These lines may result either from two overlapping powder patterns with similar principal values from the pair of slightly inequivalent methyl groups on each five-membered ring, or from a distribution of hyperfine couplings from methyl groups in slightly different conformations. However, the variation in splittings with RF pulse parameters strongly suggest that the spectra are modified by coherence splittings [20,21] or multiple quantum transient nutation effects [22]. Each trityl radical contains 36 similar, if not exactly equivalent, protons, so that excitation of proton multiple quantum coherences by the 72 μs RF pulses used in Fig. 2 is a distinct possibility.

An apparent pair of peaks with a splitting of ~100 kHz is actually a single featureless peak from residual protons in the solvent with a 'polarization hole' burned in the center. This hole is a well-characterized feature of Mims ENDOR spectra. Unlike real hyperfine splittings, the apparent splitting of this peak strongly depends on experimental parameters that determine the depth and width of the 'polarization hole.' There is also a pair of wings that extend out beyond the lobes split by ~750 kHz mentioned earlier and are the tails of the solvent or matrix ENDOR line. This is clearly seen in a sample of perdeuterated **I** in H_2O/glycerol, Fig. 2, inset. The wings of the matrix line are enhanced by the 'τ-suppression holes' or 'blind spots' characteristic of Mims ENDOR [16,23]. The ENDOR intensity is modulated by a factor roughly proportional to $(1 - \cos(2\pi A\tau))$ where A is the hyperfine splitting and τ is the separation between the first two microwave pulses in the Mims ENDOR pulse sequence. In Fig. 2, $\tau = 312$ ns and the relevant blind spots or holes appear for $|A| = 0$ or 3.20 MHz, that is, for protons at ν_p and $\nu_p \pm 1.6$ MHz,

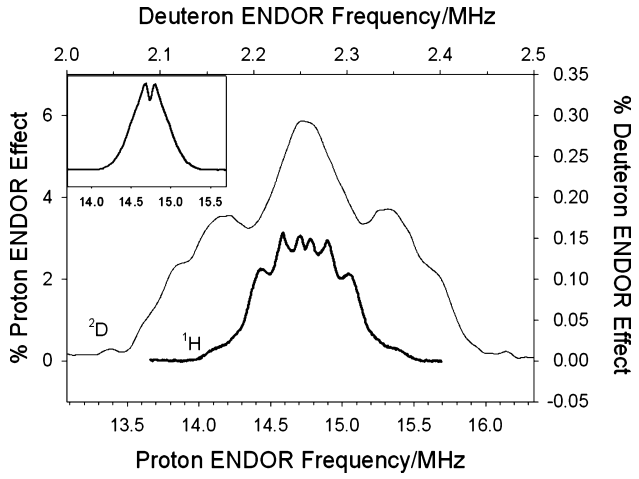

Fig. 2. The lower, darker trace is the Mims ENDOR spectrum of 1.5 mM **I** in deuterated methanol at 60 K and 346.28 mT. The pulse repetition rate was 195 Hz with 16 ns 9.705 GHz microwave pulses, and interpulse delays of 0.312 and 73 μs with a 72 μs RF pulse at a nominal power of 5 W. The solid line is the normalized ENDOR effect, $\Delta E/E$. The so-called 'τ-suppression holes' that appear in Mims ENDOR spectra lie far outside this spectral window at 11.5 and 17.9 MHz. However, there is a central hole at the proton Zeeman frequency, that enhances ENDOR lines proportional to their distance from the proton Zeeman frequency. This has the effect of unduly emphasizing the small tails from residual solvent protons near 14.1 and 15.4 MHz by a factor of 2–4 relative to the main ENDOR peaks. The ENDOR spectrum of solvent protons of 0.5 mM perdeuterated **I** in H_2O/glycerol under similar conditions is shown in the inset box. The lighter, upper trace is the deuterium Mims ENDOR spectrum of 0.5 mM perdeuterated **I** in H_2O/glycerol at 60 K and 345.13 mT. The pulse repetition rate was 98 Hz with 16 ns 9.675 GHz microwave pulses, and interpulse delays of 0.512 and 73 μs with a 72 μs RF pulse at a nominal power of 5 W. The solid line is the normalized ENDOR effect, $\Delta E/E$. The axes for the deuterium spectrum are at the top and right-hand side of the plot. The frequency scales have been adjusted by the ratio of the nuclear Zeeman frequencies to allow direct comparison. The deuterium ENDOR spectrum is approximately an order of magnitude weaker than the proton ENDOR because of the so-called 'τ-suppression hole' for the reduced hyperfine splittings.

while the full intensity is observed only at $\nu_p \pm 0.8$ MHz which is near the two edges of the spectrum in Fig. 2. The practical consequence is the partial suppression of that part of the spectrum with small couplings and the apparent 'emphasis' of the wings near $\nu_p \pm 0.7$ MHz by comparison.

The extreme ends of this matrix ENDOR line correspond to a hyperfine splitting of 1.4 MHz. If this is assigned to the parallel principal value of a purely dipolar interaction between the closest solvent proton and the unpaired electron in the point–dipole approximation, it would indicate a distance of closest approach of 0.48 nm. This would suggest steric shielding of the unpaired electron spin from the solvent in **I**.

The deuterium ENDOR spectrum of the perdeuterated **I** in a protiated solvent, Fig. 2, is much broader than would be expected simply by scaling the proton hyperfine couplings. The deuteron has a much smaller magnetic moment than the proton, which reduces the nuclear Zeeman frequency and the hyperfine couplings to 15.35% those of the protons. Yet the scaled deuterium ENDOR spectrum is more than twice the width of the proton ENDOR spectrum and the lineshapes are quite different. The reason for this difference in spectra is that the deuteron has a nuclear spin $I = 1$ and consequently a nuclear quadrupole moment while the proton with $I = 1/2$ does not. The deuterium ENDOR spectrum is ~200 kHz wider than would be expected from scaling the proton ENDOR spectrum of **I** and indicates that the quadrupole splitting is characteristic of an immobilized C–D bond rather than a freely rotating methyl group.

The deuterium ENDOR spectrum is approximately 10% of the intensity of the proton ENDOR spectrum. This decrease is caused in large part by the 'τ-suppression hole' or 'blind spot' for very small hyperfine splittings. The product $A\tau$, even with the slightly larger value of used to measure the deuterium ENDOR spectrum, is only a quarter that for the corresponding splitting in the proton ENDOR spectrum, thus producing a substantial decrease in the intensity factor $(1 - \cos(2\pi A\tau))$.

The carboxyl groups are free to exchange with the solvent and will have the same isotopic composition as the solvent. No ^{1}H or ^{2}H ENDOR peaks were observed that could be distinguished from the solvent and assigned to protons on the carboxyl groups of the trityl radical. Because of their low degeneracy and expected strong overlap with the methyl protons and solvent protons, the carboxyl protons should not be easily observed.

3.3.2. Proton coherence transfer ENDOR

The best proton ENDOR spectrum was obtained using coherence transfer ENDOR with TPPI to separate out multiple quantum contributions. The $\pi/2$ RF pulses were 3 μs wide which is too wide to completely excite the proton ENDOR spectrum, particularly in the higher multiple quantum orders. Therefore, a two-dimensional (2D) measurement was made in which the second dimension is the RF frequency. The coherence transfer ENDOR spectrum, Fig. 3, was obtained as a skyline projection of the 2D spectrum. The TPPI results in the single-quantum ENDOR spectrum appearing centered at 4 MHz, the double-quantum ENDOR spectrum at 8 MHz, and the triple-quantum ENDOR spectrum at 12 MHz as marked by the arrows. The spectrum shows spurious responses near 11.25 and 15.25 MHz apparently from coherent noise of the pulse programmer.

The single-quantum ENDOR spectrum is similar to, but broader than, the Mims ENDOR spectrum. The outer lobes of the spectrum indicate a maximum hyperfine splitting of about 1 MHz and the polarization hole produces a pair of inner lobes split by 260 kHz. The double-quantum ENDOR peak is weak and rather fea-

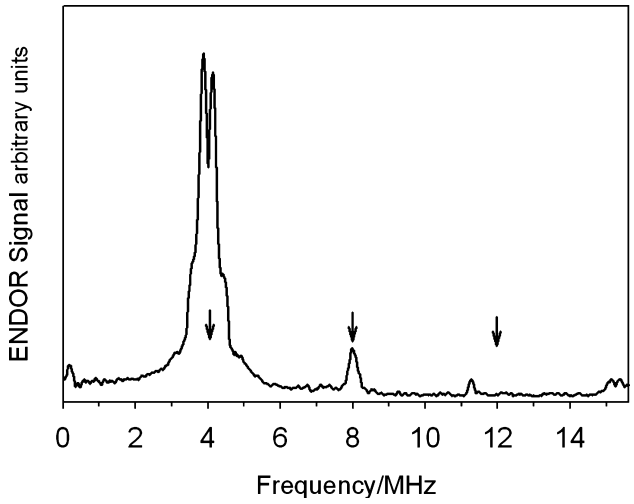

Fig. 3. Multiple quantum coherence transfer ENDOR spectrum of 1.5 mM **I** in deuterated methanol at 60 K. The multiple quantum orders are separated by 4 MHz as a result of the TPPI as described in the text. Arrows mark the expected locations of the single-, double-, and triple-quantum ENDOR spectra.

tureless and the triple-quantum peak is missing entirely. The absence of a triple-quantum ENDOR signal indicates that the protons in the methyl groups are non-degenerate and hence non-rotating. In this case, the single quantum and the Mims ENDOR spectra would be the superposition of spectra from each methyl conformer in the sample and the proton ENDOR spectrum could not be interpreted in terms of one or two hyperfine tensors for the methyl protons.

3.3.3. ^{13}C ENDOR

The ENDOR spectrum measured at the center of the intense EPR line, Fig. 4, upper trace, shows weak ENDOR signals near the ^{13}C nuclear Zeeman frequency corresponding to small hyperfine couplings of less than 0.9 MHz. The relative signs of hyperfine couplings can be determined using ENQOR spectroscopy. The ENQOR spectrum, Fig. 4, lower trace, reveals a correlation between the ^{13}C ENDOR and the proton ENDOR. Here the RF pump frequency of 14.452 MHz corresponds to the low-frequency lobe of the methyl protons. The ^{13}C ENDOR peak near 3.4 MHz has negative amplitude in this ENQOR spectrum while its partner near 4.0 MHz has positive amplitude. The ENQOR spectrum inverts when the high-frequency lobe at 14.996 MHz is pumped, indicating that the ~0.8 MHz ^{13}C hyperfine coupling and the largest hyperfine splitting of the methyl protons have opposite signs. The anisotropic part of the methyl proton hyperfine interaction is dominated by dipolar interaction with the large unpaired electron spin density at the central carbon atom as discussed later. Consequently, the largest hyperfine splitting of the methyl protons is positive and the ^{13}C hyperfine coupling in Fig. 4 of ~0.8 MHz negative.

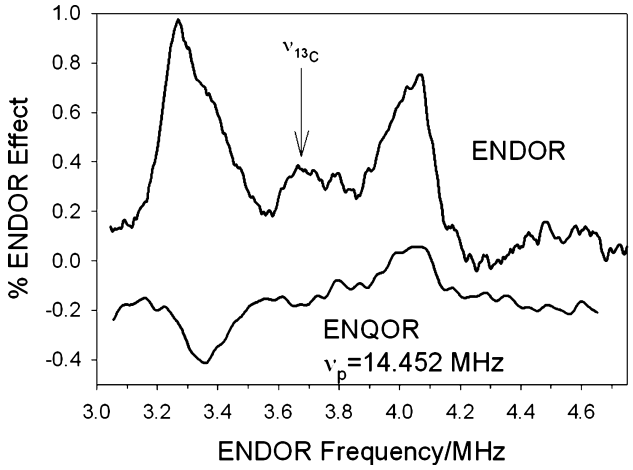

Fig. 4. (Upper trace) The Mims ENDOR spectrum of 1.5 mM **I** in perdeuterated methanol at 60 K and 346.35 mT. The pulse repetition rate was 122 Hz with 16 ns 9.705 GHz microwave pulses, and interpulse delays of 0.512 and 73 μs with a 72 μs RF pulse at a nominal power of 100 W. The spectrum is plotted as the normalized ENDOR effect, $\Delta E/E$. The nuclear Zeeman frequency of ^{13}C is indicated by the arrow at 3.676 MHz. The so-called 'τ-suppression holes' that appear in Mims ENDOR spectra lie far outside this spectral window at 1.7 and 5.6 MHz. Only the smallest hyperfine couplings are observed in this narrow scan. (Lower trace) The Mims ENQOR spectrum of the same sample using 40 μs RF pulses. The pump frequency of 14.452 MHz corresponds to the $A_{\|}$ of the methyl protons. The baseline is offset by −0.2%. The pattern in the ENQOR spectrum indicates that the ^{13}C hyperfine coupling of ~0.8 MHz and the $A_{\|}$ of the methyl protons have opposite signs.

Despite observations of large ^{13}C hyperfine couplings in CW EPR spectra, no large couplings were observed in ENDOR spectra measured at the center of the intense EPR line of **I**. This result should not be a surprise because the vast majority of radicals containing ^{13}C are only singly 'labeled.' Consequently, the radicals that are resonant at the center of the EPR spectrum have only a small or no ^{13}C hyperfine splitting. The radicals with the large couplings are split out away from the center of the EPR spectrum so that the ENDOR spectrum depends on the position in the EPR spectrum at which it is measured. This phenomenon is well known in the fields of ENDOR and ESEEM as 'orientation selection' [24]. That is, measurements made in any part of an anisotropic EPR spectrum select out a subset of radicals whose orientations, hyperfine couplings, isotopic composition, etc. satisfy the resonance condition for that specific EPR field/frequency combination. Thus in order to observe the large hyperfine couplings in the ENDOR spectrum it is necessary to make the measurement in a part of the EPR spectrum where the observed radicals have a large hyperfine coupling. This is equally true for CW ENDOR whether in the liquid or frozen state. For the larger ^{13}C hyperfine couplings, solution ENDOR has limited value because the hyperfine coupling must be determined in order to find the field position for the ENDOR measurement.

A series of ENDOR spectra, Fig. 5, measured on the high-field side of the intense EPR line demonstrate this effect. The Davies ENDOR sequence was used because it avoids the 'τ-suppression holes' of Mims ENDOR at the expense of suppressing small couplings. Microwave and RF pulse widths were shorter than absolutely necessary in order to suppress the intense proton matrix ENDOR line from the solvent and to enhance the broad, anisotropic ^{13}C ENDOR lines. This strategy was only partially successful and a large remnant of the proton ENDOR line arising from both 'labeled' and 'unlabeled' radicals remains in the spectra.

The upper traces in Fig. 5 were measured with the magnetic field close to the center of the trityl EPR spectrum where the hyperfine splittings are small. The traces toward the bottom were measured at higher fields where the splittings are larger. These traces form a 2D spectrum correlating the magnetic field (or hyperfine splitting) with the ENDOR frequency. To first order it is a linear mapping, so that the ENDOR frequency is given by $\nu = |\nu_C \pm A/2|$ for small hyperfine couplings with $\nu_C > |A/2|$, or $\nu = |A/2 \pm \nu_C|$ for $\nu_C < |A/2|$ where ν_C is the ^{13}C nuclear Zeeman frequency. Near the center of the EPR spectrum the ENDOR peaks are all confined largely to the region between 0 and $2\nu_C = 7.5$ MHz while in the lower traces the ENDOR peaks fall onto two parallel ridges separated by $2\nu_C$. In this particular type of 2D spectrum the peaks fall on top of each other and are not dispersed over two dimensions. The hyperfine tensors can only be determined from this spectrum by considering the intensity profile of the ENDOR ridges or their projections onto the ENDOR frequency axis. Some features can readily be identified, such as two perpendicular hyperfine features in the higher frequency ridge at roughly 13.5 MHz and at 17.5 MHz. The corresponding parallel hyperfine features can be identified with more difficulty near 22.0 and 24.6 MHz, respectively. However, spectral overlap and congestion becomes severe for ENDOR frequencies in the range 5.5–9.0 MHz.

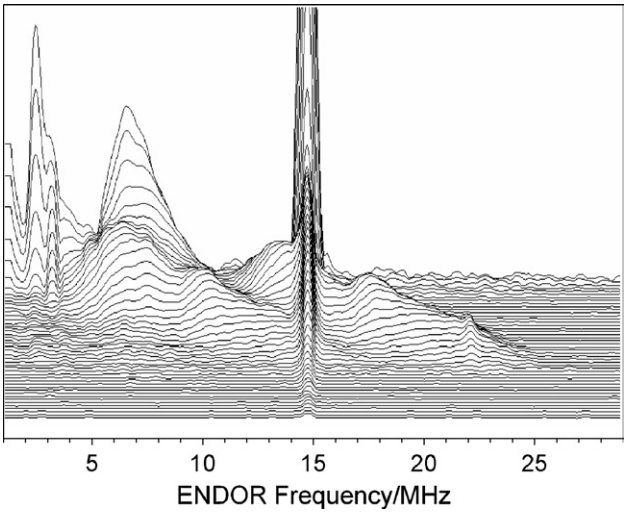

Fig. 5. The Davies ENDOR spectrum of 1.5 mM **I** in perdeuterated methanol at 60 K. The pulse repetition rate was 122 Hz with 9.703 GHz microwave pulses of lengths 128, 128, and 256 ns, and interpulse delays of 13 and 0.512 μs with a 12 μs RF pulse at a nominal power of 500 W. This plot shows a stacked plot of a series of ENDOR spectra measured at different magnetic fields starting at 346.28 mT at the top of the figure to 347.38 at the bottom with the field changing 0.0245 mT between successive traces. This range covers approximately from the center of the EPR spectrum through all of the resolved ^{13}C resolved hyperfine lines except for the most anisotropic coupling and midway out on the high field wing in Fig. 1. The Davies ENDOR method is not subject to the 'τ-suppression holes,' but does tend to discriminate against small hyperfine couplings. The strong line just below 15 MHz is the proton matrix ENDOR line from residual protons in the solvent and the line just above 2.2 MHz is the deuterium ENDOR signal. The rest of the lines in the spectrum are from the natural abundance ^{13}C in **I**.

No indication of ^{33}S ENDOR was observed. Because ^{33}S has a large quadrupole moment (comparable to that of ^{35,37}Cl), the ENDOR spectra of ^{33}S would be strongly broadened and shifted.

Most of the features in roughly 200 proton and carbon ENDOR spectra measured under different conditions could be assigned guided by the CW liquid phase and solid-state EPR spectra and calculated hyperfine tensors from the quantum chemical modeling. The experimental hyperfine tensors were approximated as axially symmetric because of the limited resolution in the spectra. The results are summarized in Table 2.

3.4. Quantum chemical modeling

3.4.1. Trityl radical

The geometry optimization of **I** with the 6-21G and 631G basis sets converged to a symmetric, propeller-shaped molecule, Fig. 6. No symmetry was imposed during optimization, but the final structure nearly has C_3 symmetry. The total energy of **I** calculated with different basis sets is listed in Table 3. Generally the calculated isotropic hyperfine couplings decrease as the quality of the basis set increases, Table 3. Good agreement between calculated and measured isotropic hyperfine couplings was achieved with the 6-311G** basis, Table 1. Average values and standard deviations are given for 'equivalent' positions.

Each carboxyl group converged to the acid form hydrogen bonded to a water molecule. The carboxyl group and associated water have the same orientation and are related by the 3-fold axis. The common orientation is probably due to the initial starting structure because a rotation of any carboxyl group and associated water by 180° (or reflection in the O–C–O plane) should have negligible effect on total energy. The carboxyl group is twisted out of the plane of the phenyl by nearly 21° caused by contacts between the oxygens of the carboxyl group and the sulfurs on the phenyl group. The

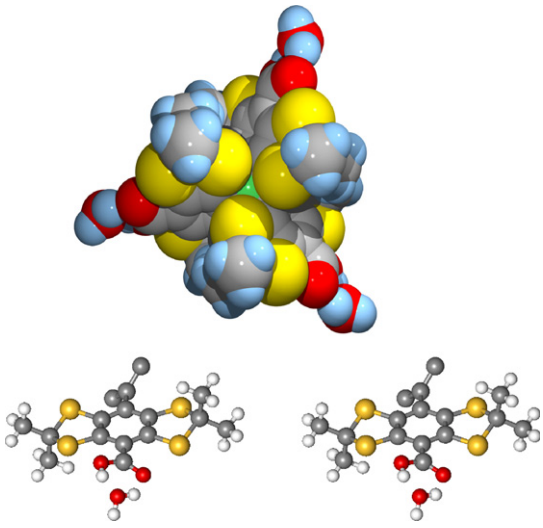

Fig. 6. (Upper) The optimized structure of **I** viewed approximately along the 3-fold axis. The central methyl carbon is colored light green to make it visible through the opening between three sulfur atoms around the 3-fold axis. (Lower) A stereoview of one of the aryl groups showing its conformation. The view also includes the central methyl group and the attached carbons from the two other aryl groups, illustrating the 'propeller' twist of the aryl groups. The structure was optimized by Gaussian 98 with the B3LYP functional and the 6-31G basis set.

oxygen–sulfur distance is 0.271 nm, which is considerably smaller than the sum of their van der Waals radii.

The two five-member rings on each phenyl group are non-planar with the bridging carbon twisted out-of-plane. In addition, the five-member rings on each phenyl group are twisted in opposite directions so that the whole substituted phenyl group is in a chair-like conformation. The bulky substituted phenyl groups are much too large for the three phenyls to be coplanar and so they are twisted. The phenyl ring is twisted by 51° relative to the plane defined by the central carbon and its three bonds. This makes the three phenyl rings nearly perpendicular to each other with an angle of 84.5° between the planes. If the carboxyl groups are ignored, this trityl radical would have D_3 symmetry.

This radical structure is more a structural model in the sense that it closely resembles most radicals in the solution, analogous to the 'NMR structure' of a protein. The lack of precise 3-fold symmetry indicates that the energy minimum does have some width. The 'structural inequivalence' of chemically equivalent groups results in a dispersion of hyperfine couplings which are reflected in Tables 1 and 2. The experimental ENDOR and frozen solution EPR spectra show '*A*-strain' from the dispersion of hyperfine tensor values from the distribution of conformations throughout the sample. In a hydrogen bonding solvent, many different opportunities for hydrogen bonds involving the carboxyl groups and the sulfur atoms are possible but are beyond the scope of these quantum chemical calculations. Fortunately, they appear not to have a strong effect on the hyperfine couplings.

Fig. 6 shows a striking feature of **I**. The central carbon is completely surrounded in a plane by the three carbons it is bonded to, while above and below that plane are close packed clusters of three sulfur atoms from three different phenyl groups. The carbons at the 1, 2, and 6 positions of the phenyl rings are completely inaccessible to solvent while there is only limited access to the carbons at the 3, 4, and 5 positions and to the sulfurs in contact with the central methyl group. As a result of this structure, most of the unpaired electron density is inaccessible to solvent. The total atomic spin densities with magnitudes greater than 0.001 calculated with the 6-311G** basis set are reported in Table 4 along with a qualitative indication of the solvent accessibility to that atom. The carbonyl oxygens on the carboxyl group have the largest spin density with good access to the solvent while the carbon at the 4-phenyl position where the carboxyl group is attached has the largest spin density among the atoms with limited solvent access.

Table 4
Average atomic spin density and solvent accessibility

Position	Atomic spin density	Degeneracy	Solvent accessible
Central methyl	0.746	1	No
1-Phenyl	−0.107	3	No
2,6-Phenyl	0.079	6	No
3,5-Phenyl	−0.035	6	Limited
4-Phenyl	0.072	3	Limited
S at 2,6-Phenyl	0.012	6	Limited
S at 3,5-Phenyl	−0.001	6	Yes
Carboxyl C	−0.004	3	Yes
Carbonyl O	0.014	3	Yes
Hydroxyl O	0.003	3	Yes

Table 3
Calculated energy and isotropic hyperfine couplings of **I** using different basis sets with the B3LYP functional

Basis set	6-21G	6-31G	6-31G**	6-311G	6-311G**	Measured
Energy/Hartree	−7003.826	−7005.738	−7006.752	−7006.607	−7007.578	—
Central Carbon	153.7	142.3	102.2	68.6	61.6	67.1
1-Phenyl	−42.75	−40.16	−31.19	−36.73	−32.51	32.09
2,6-Phenyl	37.02	34.32	28.26	28.58	25.66	25.30

Structure optimized using the 6-31G basis set except for the 6-21G calculation which was optimized with that basis.

3.4.2. Trityl radical fragment

There is significant spin density on the carbonyl oxygen of the carboxyl groups and at the phenyl carbon where the carboxyl group is attached. Consequently, the conformation of the carboxyl group relative to the phenyl ring could potentially modulate spin density, hyperfine couplings and provide a possible route for electron spin relaxation driven by solvent interactions with the carbonyl group and the sulfurs it is in contact with.

A fragment of **I** was modeled to examine the effect of carboxyl group rotation. This fragment is related to the structure in Fig. 6 by the removal of the water coordinated to the carboxyl group and the replacement of two substituted phenyl rings by protons. The dihedral angle between the phenyl ring and plane of the central carbon and its bonds was constrained to be 51°. The carboxyl group was then rotated in 15° increments and the structure was optimized with the 6-31G basis set and the properties were calculated. The unpaired spin wavefunction was similar to that calculated with the same basis set for **I** with coordinated water molecules. The isotropic hyperfine coupling on the central carbon increased about 7% because of decreased delocalization onto the two missing aryl groups while the isotropic hyperfine couplings calculated for the carbons of the phenyl ring and carboxyl group increased in magnitude by 10–30%.

In the trityl fragment, the two five-membered rings adopted a 'boat' conformation in the lowest energy structures rather than the 'chair' conformation of **I**. Apparently steric constraints from the other aryl groups favor the 'chair' conformation. The *meta* (and *ortho*) positions on the phenyl ring are not related by symmetry in the 'chair' conformation and the isotropic hyperfine couplings calculated for those carbons differ by ~15% while they are essentially identical in the full molecule.

Rotation of the carboxyl group had little effect on the unpaired spin density except on the carboxyl group itself. The isotropic hyperfine couplings of the carbons in the fragment varied by 1–2 MHz, which could broaden the ^{13}C ENDOR spectra but would not likely lead to spin relaxation particularly in radicals without ^{13}C. Paradoxically, the isotropic hyperfine coupling of the carboxyl carbon was practically invariant with carboxyl group rotation. However, the –OH proton on the carboxyl group had isotropic couplings that varied between −0.51 when coplanar and +2.45 MHz when perpendicular to the phenyl ring. Also, the unpaired spin density on the carbonyl oxygen of the carboxyl group was relatively large and varied strongly with rotation of the carboxyl group as shown in Fig. 7. The barrier for rotation of the carboxyl group is 22.3 kJ/mol, however, the minimum is fairly broad with ± 15° rotation from the minimum raising the energy by less than thermal energy at 300 K.

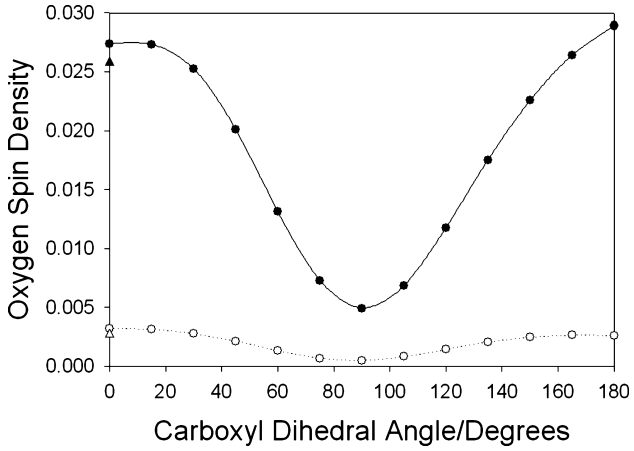

Fig. 7. Dependence of the total unpaired spin density on the carboxyl oxygens of the trityl fragment as a function of the relative orientation of the phenyl ring and carboxyl group. Calculated as discussed in text using the 6-31G basis set. The solid symbols are for the carbonyl oxygen and the open symbols for the hydroxyl oxygen. The circles are for the 'boat' conformation while the triangles are for the 'chair' conformation.

4. Discussion

4.1. Radical structure

This trityl radical, **I**, is the archetype of a class of sulfur containing, extremely stable free radicals that have narrow EPR spectra suited for magnetic resonance imaging of living systems using EPR. It is important to understand how the physical and chemical structure of this class of free radicals affects its properties for imaging. The trityl radicals, like other triaryl methyl radicals, have the potential to form a delocalized, planar aromatic system. However, steric interactions among the substituents of the aryl groups prevent the molecule from being planar and consequently disrupt the delocalization of the unpaired spin. Much of the unpaired spin density is trapped on the central methyl carbon atom with the exact amount depending on the conformation of the free radical.

There is a need to synthesize new members of the trityl family with properties better suited for particular applications. Some of the desirable properties include a narrower EPR linewidth and longer spin relaxation times, better solubility and chemical stability, modifications to target particular physiological compartments, greater response to molecular oxygen and insensitivity to other paramagnetic species and low acute and long-term toxicity. However, any modification can impact the conformation of the radical in solution and the host of properties dependent on structure. The synthesis of new trityl radicals is sufficiently arduous [25] that it is important to be able to predict, to some extent, the structure and magnetic resonance properties of a proposed synthetic target. The results on **I** presented here

indicate that quantum chemical modeling is sufficiently accurate to allow such predictions.

The excellent agreement between calculated and experimentally measured hyperfine interactions indicates that both the electronic wavefunction and the molecular structure are calculated accurately. Our success in measuring the natural abundance ^{13}C EPR and ENDOR spectra means that essentially all the unpaired spin density in **I** is represented in the experimental measurements. A glaring exception is the calculated values for the central carbon, which deviate 10–20% from the measured isotropic and the anisotropic hyperfine couplings. This is significantly worse than for any of the carbons in the phenyl rings. The central carbon–sulfur distance is 0.317 nm, less than the sum of their van der Waals radii. Any covalent character in the carbon–sulfur interaction would not be modeled well in geometry optimization with the 6-31G basis set, resulting in errors in calculated hyperfine couplings for the central carbon.

The isotropic hyperfine couplings probe the unpaired spin distribution near each atom, while the anisotropic part of the hyperfine tensor depends on the overall shape of the unpaired spin density. Thus, the wavefunction and the geometry-optimized structure calculated for **I** are accurate models for the vast majority of conformations present in the sample. Because trityl radicals share the same molecular core, it is likely that spin unrestricted DFT calculations with the B3LYP functional will correctly predict structures of other members of the trityl family using the 6-31G basis set and their hyperfine tensors using the 6-311G** basis set.

4.2. Dynamics and relaxation

The DFT calculations provide hyperfine couplings for a static structure. The methyl groups on **I** can undergo substantial motion if the rotational barriers were small compared to the sample temperature or were in a regime that supported quantum mechanical tunneling rotation. There are many examples of static, tunneling, and freely rotating methyl groups in free radicals and each type of dynamics has different effects on the ENDOR spectrum of the methyl group. If the methyl groups are static, the proton ENDOR spectrum consists of an envelope from all possible hyperfine couplings. The single structure from the DFT calculations does not reflect any interactions between the methyl groups and solvent. The methyl groups in the calculated structure are probably more ordered than in the sample. Yet the 36 calculated hyperfine tensors should generate an ENDOR spectrum that indicates the general form of the ENDOR spectrum in the limit of static methyl groups.

ENDOR spectra were simulated for each of the 36 proton hyperfine tensors from the DFT calculations using EPR-NMR and summed together to represent the case of static methyl groups. The summed spectrum, the solid, dark line in Fig. 8, was multiplied by $(1 - \cos(2\pi A\tau))$ to account for the 'blind spots' in Mims ENDOR spectra. A second spectrum was calculated in similar fashion using the tensor averages of the three proton hyperfine tensors in each methyl group. That spectrum, the dotted line in Fig. 8, represents the ENDOR spectrum expected from rapidly rotating methyl groups. A slice through the single-quantum coherence transfer ENDOR spectrum at zero offset frequency is shown as the dashed line in Fig. 8. This slice should be unaffected by the finite RF fields used in the coherence transfer ENDOR measurement. Both simulated spectra match the two lobes of the experimental spectrum at ~14.5 and ~14.9 MHz, but only the calculated spectrum for static methyl groups reproduces the wings near 14.25 and 15.20 MHz. The simulated spectra have better-resolved features than the experimental spectra. However, the simulations do not include the full conformational heterogeneity of the methyl groups or possible relaxation effects in coherence transfer ENDOR, which would serve to smear out the sharp features in the calculated spectra. The absence of any three- or higher-quantum peaks in the coherence transfer ENDOR spectrum also argues for static methyl groups because with the limited RF fields available in this study, significant three-quantum coherence intensity is expected only if the three protons have the same ENDOR frequency, which would occur only for rapidly rotating methyl groups.

The proton ENDOR spectra rule out tunneling for the methyl groups. The proton ENDOR spectrum is temperature independent in the range 4.5–60 K. Above

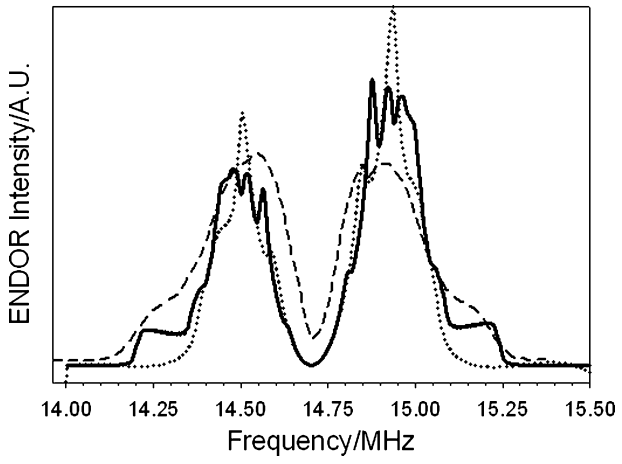

Fig. 8. Dashed line: a slice at zero offset frequency of the single-quantum coherence transfer ENDOR spectrum of 1.5 mM **I** in deuterated methanol. Dark, solid line: simulated ENDOR spectrum based on the DFT hyperfine tensors and static, non-rotating methyl groups. Dotted line: simulated ENDOR spectrum based on the DFT hyperfine tensors and rapidly rotating methyl groups as described in the text.

60 K, very slow spectral diffusion caused by motion of the radical or the solvent molecules accelerates decay of the stimulated echo sufficiently to prevent measurement of high-resolution Mims ENDOR spectra. Methyl group tunneling could not persist with such noticeable solute or solvent motion and there would be substantial changes in the EPR or ENDOR spectrum [26].

Thus, the methyl groups of **I** show no sign of motion on the ENDOR timescale of ~1 ms in frozen samples below 60 K, which is the typical temperature range for their use in DNP. In vivo oxymetry and imaging applications, however, are done at temperatures near 300 K. Space-filling models of **I** show that the methyl groups are relatively unhindered and are likely in motion at 300 K. Carboxyl group rotation, inversion of the five-membered rings, and a concerted inversion of the 'propeller' twist of **I** are distinct possibilities that would affect spin relaxation near physiological temperatures. Previous electron spin relaxation measurements on **I** reveal two different motional processes [27].

The decay rate of electron phase coherence, known variously as the spin–spin or phase memory relaxation, has a maximum in deuterated **I** that depends on solvent viscosity and was assigned to molecular tumbling of **I** [27]. There should be an additional maximum in the relaxation rate in protiated **I** when the correlation time for methyl group rotation is comparable to the proton hyperfine coupling. However, the smaller magnetic moment of deuterium makes this relaxation mechanism much less effective and more difficult to observe in deuterated **I** while the difference in mass alters the methyl group dynamics. These effects of deuteration apparently combine to prevent observation of the onset of methyl group rotation.

The second motional process was observed in the spin–lattice relaxation and was assigned to a local mode process with an energy of 590 cm^{-1} which drives relaxation at temperatures above ~100 K [27]. The spin–lattice relaxation was unaffected when the solvent went from a frozen solid to a liquid, indicating that the motion is decoupled from the solvent. Thus, the local mode probably does not involve the carboxyl group which would be hydrogen bonded to the aqueous solvent, but could involve a carbon–sulfur stretch, as originally suggested [27], inversion of the five-membered rings or inversion of the propeller pitch. All of these possibilities involve some motion of the sulfurs which surround the central carbon carrying most of the unpaired electron spin density. The sulfurs are the sites of the largest spin–orbit coupling in the radical, so that their motion would provide a mechanism for spin–lattice relaxation. It was noted [27] that spin–lattice relaxation for protiated **I** is slightly faster than for deuterated **I** at 294 K where the local mode process dominates. This observation indicates that the relaxation is not mediated by electron-nuclear-spin interaction but is consistent with a small change in the reduced mass of the groups in motion [28].

In dilute solution, **I** appears to be static at cryogenic temperatures, with non-rotating methyl groups. At physiological temperatures, the methyl groups seem to be rotating so rapidly that their rotational dynamics no longer contributes substantially to either electron spin–spin or spin–lattice relaxation. However, dynamics involving the five-membered rings does seem to determine electron spin–lattice relaxation, so that replacement of the methyl groups by bulkier groups or groups that hydrogen bond and interact more strongly with solvent should decrease the spin–lattice relaxation rate. The spin–spin relaxation at physiological temperatures and low viscosity was found earlier to be independent of molecular rotation and appears limited by the spin–lattice relaxation at X-band [27]. Replacement of the methyl groups by bulky, hydrogen bonding groups should also slow the rate of spin–spin relaxation and, because the spin–spin relaxation rate is the ultimate limit on EPR linewidth, might be expected to produce narrower EPR lines in deuterated, substituted trityl radicals for imaging and oximetry applications. However, extrapolation of X-band spin relaxation to the vastly different magnetic fields used for EPR imaging (as low as 250 MHz) or for DNP and NMR contrast agents (140 GHz or more) is risky because new spin relaxation mechanisms may become dominant at those fields.

4.3. DFT calculation of hyperfine tensors

EPR and particularly the hyperfine interaction tensors with protons and carbons provide an excellent probe of **I**. The isotropic hyperfine couplings report the unpaired spin density nucleus by nucleus throughout the radical. The anisotropic hyperfine interaction reflects the general shape of the unpaired electron wavefunction and its position relative to each nucleus. The isotropic hyperfine coupling often can be measured in liquid solutions of the free radical under conditions directly relevant to in vivo applications while the anisotropic hyperfine interaction requires measurements in the solid state, typically in frozen solutions. Modern ab initio quantum chemical programs can calculate the full hyperfine tensors rather accurately for any conformation of a free radical, so that experimental hyperfine parameters are an indication of the quality of a structural model or wavefunction.

The three largest isotropic hyperfine couplings in **I** are readily measured in liquid solution and can be tentatively assigned to particular positions based on their relative intensity or degeneracy. Table 3 shows that the DFT calculations converge on those three isotropic hyperfine couplings as the quality of the basis sets improves in much the same manner as the total energy

does. The anisotropic part of the hyperfine tensor is much less sensitive to the quality of the basis set, particularly when it is dominated by dipolar interactions with electron spin density on distant atoms. Thus, the DFT calculations can provide valuable insights into the geometry of **I** and related radicals, their electronic structure, and their electron spin relaxation properties.

Acknowledgments

This work was supported by the National Institutes of Health under Grants EB002034 and GM61904. This work was performed in part at the W.R. Wiley Environmental Molecular Sciences Laboratory, a national scientific user facility sponsored by the U.S. Department of Energy's Office of Biological and Environmental Research and located at Pacific Northwest National Laboratory, operated by Battelle for DOE. We thank Professors G. Eaton and S. Eaton for valuable discussions of their work.

References

[1] J.H. Ardenkjaer-Larsen, I. Laursen, I. Leunbach, G. Ehnholm, L.G. Wistrand, J.S. Petersson, K. Golman, EPR and DNP properties of certain novel single electron contrast agents intended for oximetric imaging, J. Magn. Reson. 133 (1998) 1–12.

[2] R.A. Wind, J.H. Ardenkjaer-Larsen, H-1 DNP at 1.4 T of water doped with a triarylmethyl-based radical, J. Magn. Reson. 141 (1999) 347–354.

[3] C.T. Farrar, D.A. Hall, G.J. Gerfen, M. Rosay, J.H. Ardenkjaer-Larsen, R.G. Griffin, High-frequency dynamic nuclear polarization in the nuclear rotating frame, J. Magn. Reson. 144 (2000) 134–141.

[4] J.H. Ardenkjaer-Larsen, B. Fridlund, A. Gram, G. Hansson, L. Hansson, M.H. Lerche, R. Servin, M. Thaning, K. Golman, Increase in signal-to-noise ratio of >10,000 times in liquid-state NMR, Proc. Natl. Acad. Sci. USA 100 (2003) 10158–10163.

[5] K.A. Rubinson, J.A. Cook, J.B. Mitchell, R. Murugesan, M.C. Krishna, S. Subramanian, FT-EPR with a nonresonant probe: use of a truncated coaxial line, J. Magn. Reson. 132 (1998) 255–259.

[6] S.K. Jackson, M.P. Thomas, S. Smith, M. Madhani, S.C. Rogers, P.E. James, In vivo EPR spectroscopy: biomedical and potential diagnostic applications, Faraday Discuss. 126 (2004) 103–117.

[7] W. Barros, P.L. De Sousa, M. Engelsberg, Low field intermolecular double-quantum coherence imaging via the Overhauser effect, J. Magn. Reson. 165 (2003) 175–179.

[8] B.B. Williams, H. Al Hallaq, G.V.R. Chandramouli, E.D. Barth, J.N. Rivers, M. Lewis, V.E. Galtsev, G.S. Karczmar, H.J. Halpern, Imaging spin probe distribution in the tumor of a living mouse with 250 MHz EPR: correlation with bold MRI, Magn. Reson. Med. 47 (2002) 634–638.

[9] R.B. Clarkson, B.M. Odintsov, P.J. Ceroke, J.H. Ardenkjaer-Larsen, M. Fruianu, R.L. Belford, Electron paramagnetic resonance and dynamic nuclear polarization of char suspensions: surface science and oximetry, Phys. Med. Biol. 43 (1998) 1907–1920.

[10] A. Blank, C.R. Dunnam, P.P. Borbat, J.H. Freed, High resolution electron spin resonance microscopy, J. Magn. Reson. 165 (2003) 116–127.

[11] P. Kuppusamy, P.H. Wang, M. Chzhan, J.L. Zweier, High resolution electron paramagnetic resonance imaging of biological samples with a single line paramagnetic label, Magn. Reson. Med. 37 (1997) 479–483.

[12] H.J. Halpern, D.P. Spencer, J. Vanpolen, M.K. Bowman, A.C. Nelson, E.M. Dowey, B.A. Teicher, Imaging radio-frequency electron-spin-resonance spectrometer with high-resolution and sensitivity for in vivo measurements, Rev. Sci. Instrum. 60 (1989) 1040–1050.

[13] R.V. Pound, Frequency stabilization of electronically tunable microwave oscillators, in: Technique of Microwave Measurements (Anonymous), McGraw-Hill, New York, 1947, pp. 58–78.

[14] P. Höfer, Multiple quantum pulsed ENDOR spectroscopy by time proportional phase increment detection, Appl. Magn. Reson. 11 (1996) 375–389.

[15] A. Schweiger, New trends in pulsed electron spin resonance methodology, in: L. Kevan, M.K. Bowman (Eds.), Modern Pulsed and Continuous-Wave Electron Spin Resonance, Wiley, New York, 1990, pp. 43–118.

[16] A. Grupp, M. Mehring, Pulsed ENDOR spectroscopy in solids, in: L. Kevan, M.K. Bowman (Eds.), Modern Pulsed and Continuous-Wave Electron Spin Resonance, Wiley, New York, 1990, pp. 195–230.

[17] M.K. Bowman, A.M. Tyryshkin, Electron nuclear quadruple resonance for assignment of overlapping spectra, J. Magn. Reson. 144 (2000) 74–84.

[18] M.J. Frisch, G.W. Trucks, H.B. Schlegel, G.E. Scusiera, M.A. Robb, J.R. Cheeseman, V.G. Zakrzewski, J.A. Montgomery Jr., R.E. Stratmann, J.C. Burant, S. Dapprich, J.M. Millam, A.D. Daniels, K.N. Kudin, M.C. Srain, O. Farkas, J. Tomasi, V. Barone, M. Cossi, R. Cammi, B. Mennucci, C. Pomelli, C. Adamo, S. Clifford, J. Ochterski, G.A. Petersson, P.Y. Ayala, Q. Cui, K. Morokuma, P. Salvador, J.J. Dannenberg, D.K. Malick, A.D. Rabuck, K. Raghavachari, J.B. Foresman, J. Cioslowski, J.V. Ortiz, A.G. Baboul, B.B. Stefanov, G.L.A. Liu, P. Piskorz, I. Komaromi, R. Gomperts, R.L. Martin, D.J. Fox, T. Keith, M.A. Al-Laham, C.Y. Peng, A.C.M. Nanayakkara, P.M.W. Gill, B. Johnson, W. Chen, M.W. Wong, J.L. Andres, C. Gonzalez, M. Head-Gordon, E.S. Replogle, J.A. Pople, Gaussian 98 (Revision A.11.), Gaussian Inc., Pittsburgh, PA, 2001.

[19] C. Mailer, B.H. Robinson, B.B. Williams, H.J. Halpern, Spectral fitting: the extraction of crucial information from a spectrum and a spectral image, Magn. Reson. Med. 49 (2003) 1175–1180.

[20] J.H. Freed, D.S. Leniart, J.S. Hyde, Theory of saturation and double resonance effects in ESR spectra. III. rf coherence and line shape, J. Chem. Phys. 47 (1967) 2762.

[21] A.E. Stillman, R.N. Schwartz, Theory of electron spin echoes in nonviscous and viscous liquids, in: L. Kevan, R.N. Schwartz (Eds.), Time Domain Electron Spin Resonance, Wiley-Interscience, New York, 1979, pp. 153–194.

[22] C. Gemperle, A. Schweiger, R.R. Ernst, ESR-detected nuclear transient nutations—detection schemes and applications, Chem. Phys. Lett. 145 (1988) 1–8.

[23] H. Thomann, M. Bernardo, Advances in electron nuclear double resonance spectroscopy, in: R.E. Botto, Y. Sanada (Eds.), Magnetic Resonance of Carbonaceous Solids, American Chemical Society, Washington, 1993, pp. 65–90.

[24] S.A. Dikanov, Yu.D. Tsvetkov, Electron spin echo envelope modulation (ESEEM) spectroscopy, CRC Press, Boca Raton, FL, 1992.

[25] T.J. Reddy, T. Iwama, H.J. Halpern, V.H. Rawal, General synthesis of persistent trityl radicals for EPR imaging of biological systems, J. Org. Chem. 67 (2002) 4635–4639.

[26] A.R. Sornes, N.P. Benetis, R. Erickson, A.S. Mahgoub, L. Eberson, A. Lund, Effect of isotopic substitution on the electron spin dynamics of the Ch3(C)˙(COOH)(2) radical in X-irradiated

methyl malonic acid powder: intrinsic potentials and activation energies, J. Phys. Chem. A 101 (1997) 8987–8994.
[27] L. Yong, J. Harbridge, R.W. Quine, G.A. Rinard, S.S. Eaton, G.R. Eaton, C. Mailer, E. Barth, H.J. Halpern, Electron spin relaxation of triarylmethyl radicals in fluid solution, J. Magn. Reson. 152 (2001) 156–161.
[28] M.K. Bowman, L. Kevan, Electron spin lattice relaxation mechanism of radiation produced trapped electrons and hydrogen atoms in aqueous and organic glassy matrices: modulation of electron nuclear dipole interaction by tunneling modes in a glassy matrix, Faraday Discuss. 63 (1978) 7–17.